Journal of Luminescence 192 (2017) 818–826

Contents lists available at ScienceDirect

Journal of Luminescence

journal homepage: www.elsevier.com/locate/jlumin

Effects of microwave-assisted hydrothermal treatment and of use of capping reagent on the photophysical properties of $SrMoO_4$ phosphors

Sidney M.V. Paradelas[a], Rosana F. Gonçalves[a], Fabiana V. Motta[b], Renata C. Lima[c], Maximo S. Li[d], Elson Longo[e], Ana Paula de A. Marques[a,*]

[a] Departamento de Ciências Exatas e da Terra, UNIFESP, CEP 09972-270 Diadema, SP, Brazil
[b] Departamento de Engenharia de Materiais, UFRN, CEP 59072-970 Natal, RN, Brazil
[c] Instituto de Química, UFU, CEP 38400-902 Uberlândia, MG, Brazil
[d] Instituto de Física de São Carlos, USP, CEP 13566-590 São Carlos, SP, Brazil
[e] LIEC, Departamento de Química, UFSCar, CEP 13565-905 São Carlos, SP, Brazil

ARTICLE INFO

Keywords:
Optical properties
Microwave processing
Chemical syntheses
Microstructure-final
Transition metal oxides

ABSTRACT

Strontium molybdate particles ($SrMoO_4$) with uniform shapes have applications in various fields such as phosphors, optical fibers, scintillators, magnets, sensors, and catalysts. $SrMoO_4$ were prepared by Microwave-Assisted Hydrothermal (MAH) method with variations in applied experimental parameters. The effect of the applied synthesis methodology and experimental parameters on the morphology, particle size, sample uniformity and optical properties of the $SrMoO_4$ were studied. In this study, was observed that the microwave radiation favors an organization of material and that this organization can be changed with a capping agent, which provokes alterations in morphology, a disorder-order degree of material and variations of band gap energy. This study indicates that surface defect states favor an alteration in properties of the PL emission. The control of a surface state, the particle size and morphology can be a form to modify the property in accordance with optics characteristics the desired one.

1. Introduction

Strontium molybdate ($SrMoO_4$), with a scheelite-type crystalline structure, are known to be wide band gap oxide semiconductors (3–5 eV). $SrMoO_4$ have wide potential and practical applications in many fields, e.g. use as phosphors, laser materials, optical detectors, scintillators, solid-state optical laser, optical fibers, humidity sensor, gas sensor, a drug carrier, magnetic materials, and catalysts [1–6].

$SrMoO_4$ micro and nano-particulate scale were used as the base in a gas sensor for monitoring of gas sulfur species. In this recent work, Ciftyürek et al. showing that hydrothermally synthesized nano-$SrMoO_4$ showed the highest sensor response [2]. The high sensor response values and stable and smooth response characteristics were attributed to the presence of these two defect states: high concentration of oxygen vacancies and oxygen interstitials. This was further supported by the difference in sensor response kinetics between the micro-$SrMoO_4$ and nano-$SrMoO_4$, where the final microstructure of each was similar after testing. This research confirms the necessity of study of the synthesis.

Strontium molybdate can be synthesized by using different techniques; however, production with single crystalline structures and controlled morphology requires caution. The conventional solid-state reaction method is frequently used to obtain molybdate powders; this method produces materials with a large grain size and irregular morphology due to high annealing temperatures and long reaction times. In addition, the tendency for MoO_3 to vaporize at high temperatures can result in non-homogeneous morphologies and compositions [7]. Several other techniques have been employed to obtain materials similar to $SrMoO_4$: Czochralski Method [8,9], Conventional Solid State Reaction Method [10], Complex Polymerization Method [11], Hydrothermal Process (autoclave) [12], Solvothermal Method [13], and Microwave Irradiation Method [1,14]. Nevertheless, some of these methods have disadvantages with high synthesis temperatures and long reaction times which destroys the morphological homogeneity.

The hydrothermal route was used by Ciftyürek et al. to produce nano-$SrMoO_4$ with nanoflowers morphology; nanoflowers-$SrMoO_4$ showed higher sensor response than micro-$SrMoO_4$ commercial [2]. In this present work, the synthesis of SMO samples was made by Microwave-Assisted Hydrothermal (MAH) Method. In MAH method a hydrothermal and a microwave irradiation are combined to produce ideal nanometric material with appropriate morphologies. The microwave

* Corresponding author.
E-mail addresses: apamarques@hotmail.com, apamarques@unifesp.br (A.P.d.A. Marques).

http://dx.doi.org/10.1016/j.jlumin.2017.08.016
Received 12 October 2016; Received in revised form 3 August 2017; Accepted 6 August 2017
Available online 11 August 2017

energy accelerates the formation of well-organized nanostructures, Microwave energy is a form of electromagnetic energy with the frequency range of 300 MHz to 300 GHz. Microwave heating is a process in which the materials combine with microwaves, absorb the electromagnetic energy volumetrically, and transform into heat. In conventional thermal treatment, a heat is transferred between objects by the mechanisms of conduction, radiation, and convection, the surface of material is first heated followed by the heat moving inward. Microwave heating generates heat within the material first and then heats the entire volume [15–17]. MHA is an attractive growth method for single crystals which provides advantages such as low synthesis temperatures and uniform rapid heating.

Studies have shown that some experimental parameters, (including the use or absence of a capping reagent and the applied synthesis methodology) caused alterations in morphologies and particles sizes, and, consequently, influenced properties of the final products as well. Therefore, in this study, the MAH method was used to obtain $SrMoO_4$ structures, which is a fast, simple and efficient soft chemical route to prepare complex oxide materials. Various complementary characterization techniques were used, including XRD, FTIR spectroscopy, Raman spectra and PL spectroscopy. FE-SEM was used to detect particles sizes and molybdate morphologies. Based on experimental results, in this study, it is proposed that the synthesis method and applied experimental parameters can modify PL properties in accordance with the optical desired properties.

2. Experimental

2.1. Materials

All chemical reagents are analytical grade and were used without further treatments: molybdenum trioxide (MoO_3) (Alfa Aesar, 99.95%), strontium acetate ($((CH_3CO_2)_2Sr)$ (Alfa Aesar, 99%), citric acid ($H_3C_6H_5O_7$) (Mallinckrodt, 99%), and four different surfactants: polyethylene glycol ($HOCH_2CH_2OH$) Mw 200, 400 and 600 (PEG 200, PEG 400 and PEG 600, respectively) and *N*-cetyltrimethylammonium bromide (CTAB) (Sigma-Aldrich, 99.9%).

2.2. Synthesis of strontium molybdate ($SrMoO_4$) by the MAH Method

Molybdenum trioxide (5×10^{-3} mol) was dissolved in approximately 50 mL of distilled water with vigorous stirring. Then, ($(CH_3CO_2)_2Sr$) (5×10^{-3} mol) was added under constant stirring. The pH of the solution was adjusted to 12 by adding KOH. Surfactant (PEGs or CTAB) was added to the system which required a capping reagent. In one of reaction systems (SMO-1), the solid sample was collected in this phase without the use of surfactant; an SMO-1 sample was washed with water and ethanol and dried at 60 °C. The other samples obtained were heat-treated using the MAH method. In SMO-2 the capping reagent was not used, SMO-3, SMO-4, SMO-5 and SMO-6 requested capping reagent PEG-200, PEG-400, PEG-600, and CTAB, respectively. To heat treatment using the MAH method, the reaction systems were transferred into a sealed Teflon autoclave and placed in a domestic microwave (2.45 GHz, maximum power of 800 W), heat-treated at 100 °C for 16 min with a heating rate fixed at 100 °C/min. The pressure in the sealed autoclave was stabilized at 2.0 atm. The autoclave was cooled to room temperature naturally, and the resulting white precipitate was collected, washed with water and ethanol and dried at 60 °C.

2.3. Characterization of $SrMoO_4$ samples

The obtained samples were characterized by XRD using a Rigaku-DMax/2500PC (Japan) with Cu-Kα radiation (λ = 1.5406 Å) in the 2θ range from 5° to 75° with a 0.02°/min increment. Lattice parameters and unit cell sample volumes were calculated using a least-square refinement REDE93 program. The average crystallite diameter (Dcrys) of the materials after heat treatment was determined by XRD results using the (112) diffraction peak of the $SrMoO_4$ phase where 2θ is located at around 27.6° according to the procedure described elsewhere [18]. The morphology and particle sizes of the as-prepared samples were observed using FE-SEM (Jeol JSM 6330F). The FT-IR spectrum was recorded with a Bruker Equinox-55 instrument. Infrared spectroscopy was used to monitor the bonding changes occurring after the synthesis process, using the KBr pellet technique. Raman spectra were recorded, in the 100–1000 cm^{-1} range, using a Raman Renishaw microscope, InVia model, with multichannel CCD detector and He-Ne laser (632.8 nm), set to 0.17 mW at the sample. Automatic cosmic ray removal option was used. The optical reflectance was measured in the wavelength range of 200–800 nm, using a UV–Vis–NIR Cary 5 G spectrophotometer. PL data was recorded at room temperature using a U-1000 Jobin-Yvon double monochromator coupled with a cooled GaAs photomultiplier and a conventional photon counting system. The 350.7 nm exciting wavelength of an argon-ion laser was used; the laser maximum output power was maintained within 25 mW. All measurements were taken at room temperature.

3. Results and discussion

Table 1 lists methods used for the $SrMoO_4$ synthesis. In the Czocharalski [8,9] and Conventional Solid State Reaction Methods [10], high temperatures and long time periods were required for the production of this material; with a difference in the state of material, one produced a crystal and the other produced powder, respectively. Marques et al. [11]. performed the calcinations at a lower temperature (above 450 °C), using a soft chemical process, displaying a high chemical homogeneity but the reaction time is much larger when compared to the MAH method. The production of binary oxide by Hydrothermal Process (autoclave) [12] used low temperature (180 °C) but the autoclave and high reaction times were needed, similar conditions were also required in the Solvothermal Method using additionally a surfactant, the oleic acid [13]. Sczancoski et al. [14]. and Thongtem et al. [1]. obtained $SrMoO_4$ phase using Microwave Irradiation Method and surfactant polyethyleneglycol, but with temperatures (140 °C) and reaction times (5 and 0.33 h, respectively) higher than used in this work and without variation of surfactant. In this present study, mild conditions were used for material preparation as compared to the literature: at 100 °C for 16 min (0.27 h) using the MAH method, therefore, low temperatures and short reaction times, which results in a synthesis process at low cost; additionally, the use of different capping agent can provoke variations in morphology and consequently variations in properties of samples.

XRD patterns of products synthesized are shown in Fig. 1. All samples have scheelite-type crystalline structure without an additional phase or impurities. Peaks observed in Fig. 1(a, b) can be indexed to the tetragonal $SrMoO_4$ phase which is in agreement with standard data from JCPDS card No. 08-0482 [19]. Table 2 compared 2θ diffraction angles and intensities of principals peaks of $SrMoO_4$ samples and JCPDS 08-0482 standard values. Both data, diffraction angles and intensities,

Table 1
Strontium molybdate (SMO) synthesis methods.

Method	Temperature (°C)	Time (h)
Czochralski Method [8,9]	1100 – 1200	30 – 40
Conventional Solid State Reaction Method [10]	900	3
Complex Polymerization Method [11]	400–500	2
Hydrothermal Process (autoclave) [12]	180	10
Solvothermal Method [13]	180	12
Microwave Irradiation Method [14]	140	5
Microwave Irradiation Method [1]	not specified	0.33
MAH method[a]	100	0.27

[a] This work.

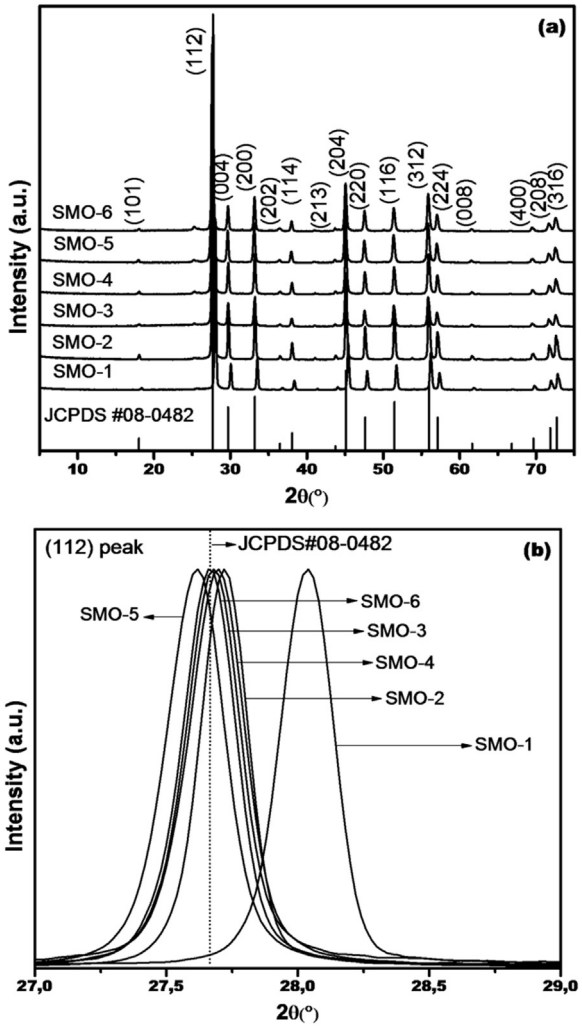

Fig. 1. XRD patterns of the SMO samples and JCPDS card (a); XRD patterns (normalized) that fall within the angle range of 27° ≤ 2θ ≤ 29° (b).

Table 2
The principals 2θ diffraction angles (°) and intensities (%) of $SrMoO_4$ obtained from in this work and JCPDS card [19].

$SrMoO_4$	2θ/Intensity (°)/ (%) Plane			
	(112)	(004)	(200)	(204)
JCPDS [19]	27.66/100	29.70/16	33.18/20	45.12/30
SMO-1	28.04/100	30.06/16	33.52/18	45.42/28
SMO-2	27.72/100	29.74/16	33.22/18	45.12/25
SMO-3	27.68/100	29.70/16	33.18/18	45.12/25
SMO-4	27.70/100	29.72/15	33.20/19	45.10/26
SMO-5	27.62/100	29.64/15	33.12/18	45.00/25
SMO-6	27.66/100	29.68/14	33.16/19	45.04/26

are in good accordance with the JCPDS standard, and all peaks were detected in the experimental results. The intensities of all diffraction peaks were close to standard data, this fact indicates that, although a change in morphology occurs, the orientations of crystal growth are the same. Diffraction of SMO-1 samples showed the peaks dislocated to largest angle values (Fig. 1(b)). It is notorious also that the use of capping agent linked with MAH treatment can promote discrete dislocations in the peaks positions to lower angles, the change in angle values is of around 0.4° (Fig. 1(b)). As calculated values of lattice parameters and crystallite size depend on diffractions angles,

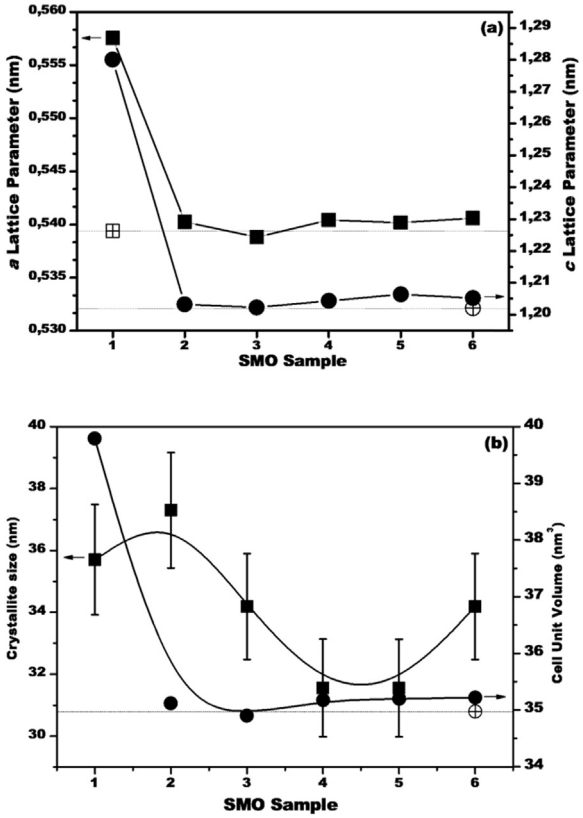

Fig. 2. Data obtained from the XRD patterns: Lattice parameters *a* (■) and *c* (•) of the SMO samples and of JCPDS card [19] (⊞ and ⊕, respectively) (a); Crystallite size (■) and unit cell volume (•) values of SMO samples and JCPDS card [19] (⊞) (b).

alterations of both, in agreement with the variation of the angle, are expected (Fig. 2). From the diffractions angles displayed in Fig. 1, lattice parameters and cell unit volumes were calculated using a least-square refinement REDE93 program, and the average sample crystallite size (D_{crys}) was determined using the (112) diffraction peak (2θ around 27.7) according to the Scherrer equation (Eq. (1)) [20]:

$$B = \kappa \times \lambda/(D_{crys} \times \cos\theta), \quad (1)$$

where B is the full width at half maximum (FWHM), κ is a constant, λ is the wavelength of the Cu Kα radiation and θ is the Bragg angle. Fig. 2(a, b) shows the cell unit volume, crystallite size and calculated lattice parameters (*a* and *c*). In Fig. 2(b) was used a fitting curve to illustrate the trend of changing the parameters. Table 3 lists cell volume values and lattice parameter values obtained in this study and a comparison with values reported in the literature and JCPDS card [1,4,14,19].

The *a* and *c* lattice parameters for these $SrMoO_4$ powders are also close to bulk material lattice parameters of JCPDS card (a = 5.394 Å and c = 12.02 Å) [19]. However, small differences in lattice parameters were observed in samples of SMO and can be related to residual stresses induced by hydrothermal preparation conditions and use of capping reagent. The synthesis of SMO-1, the absence of a capping reagent and of hydrothermal conditions seem to invoke an increase in the *a, c* and *c/a* lattice parameters in comparison with other data. In fact, the pressure of reaction system on hydrothermal conditions is a little bit greater than in open reaction system, and, the introducing of the proper surfactant (capping reagent) in the synthetic process turns to be an effective way to control the growth of crystals. Both facts can provoke alterations in structure because of the residual stresses induced in systems, according to influence in their properties [13].

The unit cell volume and crystallite size values of SMO are obtained from XRD data is shown in Fig. 1. The unit cell volumes were calculated from the product of the crystalline structure scheelite-type parameters,

Table 3
Crystallite sizes, unit cell volume (a^2Xc), comparison of tetragonal lattice constants of tetragonal structure and band gap energy values of $SrMoO_4$powders [19].

Method	Crystalline size[a]	Lattice Parameters				
	(nm)	a = b (Å)	c (Å)	a^2Xc (Å^3)	c/a	E_g (eV)
JCPDS 08-0482 [19]	–	5.394	12.02	349.8	2.228	–
Complex Polymerization Method [11]	22	5.394	12.08	351.5	2.239	–
Microwave Irradiation Method [14]	41.16	5.380	11.99	347.0	2.227	3.98
Microwave Irradiation Method [1]	16.44	5.394	12.02	349.7	2.228	–
SMO-1[b]	36(± 2)	5.575	12.80	397.8	2.296	3.49
SMO-2[b]	37(± 2)	5.402	12.03	351.0	2.227	3.46
SMO-3[b]	34(± 2)	5.388	12.02	348.9	2.231	3.36
SMO-4[b]	31(± 2)	5.404	12.04	351.6	2.228	3.75
SMO-5[b]	31(± 2)	5.402	12.06	351.9	2.233	3.87
SMO-6[b]	34(± 2)	5.406	12.05	352.2	2.229	3.69

[a] Calculated using the (112), 100% diffraction peak.
[b] This work.

in which $a = b$ and volume $= a^2Xc$ (Fig. 2b). Unit cell volumes of SMO-2 to SMO-6 (348.9–352.2 Å^3) were very close to the unit cell volume value of the JCPDS card, around of 349.8. Å^3, similar to values of unit cell volumes of $SrMoO_4$ synthesized by other methods (Table 3). SMO-1 was slightly bigger (397.8 Å^3). These observations demonstrate that the crystal can be anisotropically grown depending on the method employed. Crystallite size (D_{crys}) values of $SrMoO_4$ calculated by using Scherrer's equation were 36 nm (± 2); 37 nm (± 2); 34 nm (± 2); 31 nm (± 2); 31 nm (± 2) and 34 nm (± 2) for SMO-1, SMO-2, SMO-3, SMO-4, SMO-5 and SMO-6, respectively. The results were close to the results of Sczancoski et al. [14], Wang et al. [4] and Marques et al. [11,21], among others. Fig. 2b showed clearly that the effect of pressure caused by hydrothermal conditions favors the increase of crystallite (SMO-2), it probably occurs because with the increase of pressure the crystallite nucleus approaches and favors the rise of crystalline size. When the capping reagent is introduced into the reaction system it promotes the spacing of crystallite nucleus generating particles with smaller crystallite size (SMO-3 to SMO-6).

The influence of the pressure on hydrothermal conditions and the introducing of the surfactant (capping reagent) in the control the growth of crystals can be visible in FE-SEM micrographs (Fig. 3). Syntheses using MAH method occur in the liquid phase where the crystalline unit can grow freely in any direction (3D); therefore, it is expected that the use of capping reagent can control the growth and type of final morphology. FE-SEM images of SMO-2 to SMO-6 samples (see Fig. 3(b-f)) as compared with SMO-1 (see Fig. 3(a)) proves that parameters used during a hydrothermic treatment (the higher pressure, the use of microwaves radiation, the presence of capping reagent and the increase of temperature) can produce modifications in the morphology.

Micrographs of SMO-1 and SMO-2 samples showed primarily octahedral morphologies which get interconnected to form sort of coral sea crystals (see Fig. 3(a,b)). The use of hydrothermal parameters, in the absence of capping reagent (SMO-2), favors the presence of structures with distortions in micro-octahedra with a shortening of shapes (Fig. 3(b)). The process of the growth considered for these crystals indicates that the growth occurs for “self-assembly” of Nano-metrics small crystals, and the further growth of bigger and intermediate structures leads to the formation of sort of coral sea crystals.

The aggregates were better controlled with the use of capping reagent and hydrothermal parameters (Fig. 3(c-f)). The capping reagent hinders an approximation of micro-octahedra neighbor and therefore inhibits the formations of a larger structure (formation of sort of coral sea crystals), leads to a formation of sort of type tied sticks-, sea urchin-, feather- crystals and favors a maintenance of primary octahedral-crystals too. The bigger the chain of the capping reagent is kept easier a primary octahedral form. Therefore, processing conditions and the use of a capping reagent are very important in the crystal growth process.

The SMO powders have tetrahedral symmetry (T_d), in this representation, only the $F_2(\nu_3, \nu_4)$ modes are IR active. The $F_2(\nu_3)$ vibrations are the antisymmetric stretches, and the $F_2(\nu_4)$ vibrations are bending modes. The spectra of the all samples SMO display a very broad absorption band between 830 and 840 cm^{-1}. These bands are assigned to $F_2(\nu_3)$ antisymmetric stretch vibrations, referring to the Mo–O stretching vibration in MoO_4^{2-} tetrahedral [22]. The band referring to $F_2(\nu_4)$ vibration mode (~400 cm^{-1}) is not observed in the SMO due to a limitation of equipment.

Sample Raman spectra is shown in Fig. 4 and the Raman mode frequencies are detailed in Table 4, according to Basiev [8], where the $SrMoO_4$ primitive cell includes two internal and external groups, where one is referring to the strong covalent Mo-O bonds and other to the motions and free rotation of Sr^{2+} and $[MoO_4]^{2-}$, respectively. The presence of strong covalent Mo-O bonds was discussed by Thongtem et al. [1] based on a function of the crystal-field splitting and hybridization of the molecular orbitals of $[MoO_4]^{2-}$ tetrahedrons.

Second Thongtem et al. [1] the Mo 4d(t_2) and Mo 4d(e) orbitals are hybridized with the O 2p(σ) and O 2p(π) ligand orbitals to form $[MoO_4]^{2-}$ tetrahedrons in $SrMoO_4$ structure. The four ligand p(σ) orbitals are compatible with the tetrahedral representation for a_1 and t_2 symmetries, and the eight ligand p(π) orbitals are for t_1, t_2, and *e* symmetries. The Highest energy Occupied Molecular Orbital (HOMO) has t_1 symmetry formed from O 2p(π) states. The Lowest energy Unoccupied Molecular Orbital (LUMO) has *e* symmetry formed from a combination of the Mo 4d(*e*) and O 2p(π) orbital to give anti-bonding (*). The hybridizations between the Mo 4d and O 2p are specified as covalent bonding between the ions. $[MoO_4]^{2-}$ tetrahedrons were observed in Raman spectra, designated as MoO_4^{-2} external modes.

The Raman spectra displays three sets of defined peaks around of $100-200$ cm^{-1}, $300-400$ cm^{-1} and $750-900$ cm^{-1} corresponding to MoO_4^{-2} external modes and Sr^{2+} motions and free rotation; ν_2 (*E*) and ν_4 (F_2); and ν_3 (F_2) and ν_1 (A_1) Raman modes, respectively. Raman data for all sample showed intense and defined peaks in the third and second sets and with loss definition in the first set.

SMO-1 to SMO-6 samples showed scheelite-type phases by DRX, Raman, and FTIR data. However, for a perfect crystal, the first-order Raman phonon spectrum consists of narrow lines that correspond to Raman-allowed zone center (Γ-point) modes, definite polarization selection rules. Raman spectra for SMO illustrates samples with disordered-ordered levels because they showed an appearance of broad Raman bands reflecting the phonon density of states proportional to the lattice expansion [8,23,24]. In Basiev [8] it was mentioned that the bandwidth of $\nu_1(A_g)$ Raman mode depends on the peculiarities of a crystal lattice. Therefore, a $\nu_1(A_g)$ mode frequency increases with lattice expansion and a consequent growth in this Mo-Mo distance in the scheelite, as observed in this work.

The FWHM values from Bragg reflections and Raman bands were calculated to SMO samples and are summarized in Table 5. If narrow lines are characteristics of an ordered crystal, as discussed previously, the line width values in this work demonstrate that these materials have slightly different levels of deep defects which depend upon thermal treatment and the addition of a capping reagent. Results in Table 5 demonstrated that SMO-1 material was the less ordered by Raman but this result was not confirmed by XRD, SMO-5 present less ordered by XRD. However the limit of the XRD measure is 0.02°, therefore, the values of FWHM between the samples were practically equivalent. The material with minor FWHM by Raman and XRD was SMO-2, therefore, this was the material ordered the most. Minor FWHM by XRD is generated when the atom or molecules occupy the same positions (more

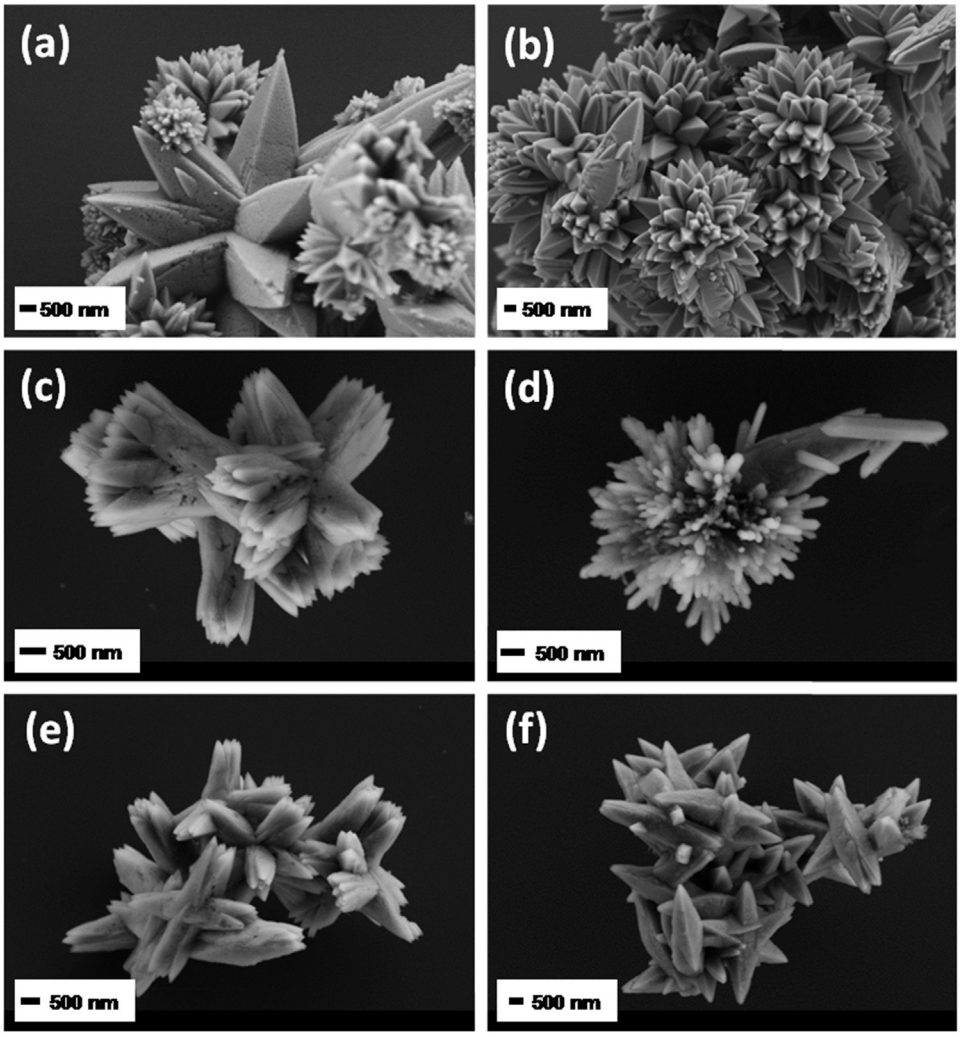

Fig. 3. FE-SEM micrographs of $SrMoO_4$ crystals prepared by MAH, SMO-1 (a), SMO-2 (b), SMO-3 (c), SMO-4 (d), SMO-5 (e) and SMO-6 (f).

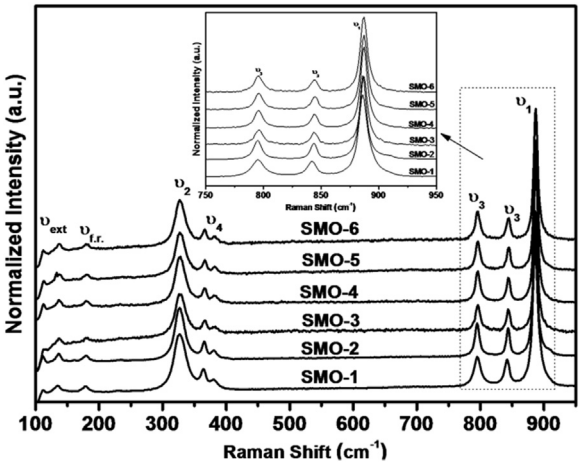

Fig. 4. Spontaneous Raman spectra of SMO samples.

Table 4
Raman mode frequencies in $SrMoO_4$ powders prepared at different temperatures.

Lattice mode symmetry C_{4h}^6	$SrMoO_4$						Assignments
	SMO-1	SMO-2	SMO-3	SMO-4	BMO-5	BMO-6	
Ag	886	886	887	888	887	887	ν_1 (A_1)
Bg	842	844	844	844	845	845	ν_3 (F_2)
Eg	795	795	796	796	796	796	
Eg	379	380	381	382	382	382	ν_4 (F_2)
Bg	364	365	366	366	366	366	
Bg	327	327	327	328	327	327	ν_2 (E)
Ag							
Eg	179	179	181	180	181	181	$\nu_{f.r.}$ (F_1) free rotation
Eg	135	136	138	137	136	138	$\nu_{ext.}$ – external Modes MoO_4^{2-} and Sr^{2+} motions
B_g	111	112	115	112	113	113	

organized) with a higher frequency and present more intense peaks (more crystalline regions with same organization, more similar positioning). Again, the effect of pressure caused by hydrothermal conditions favors the increase of crystallite (SMO-2) and consequently increases the order of the system. When the capping reagent is introduced into the reaction system it promotes the spacing of crystallite nucleus generating particles with smaller crystallite size and less order (SMO-3 to SMO-6). The absence of higher pressure is effective to obtain more disordered materials, where the order occurs naturally. However, these characterization techniques did not facilitate a study of material energy levels. Optics techniques, as a reflectance diffuse and photoluminescence spectroscopy, are indicated tools to reach this objective.

In this research, all samples were characterized by scheelite structure, which was expected, however with a different disorder-order

Table 5
Full width at half maximum (FWHM) and intensity percentage obtained through Raman and XRD data of the SMO powders.

Peak data	Sample					
	SMO-1	SMO-2	SMO-3	SMO-4	SMO-5	SMO-6
	FWHM of Raman peak (Intensity) (units: cm^{-1} (%))					
887(ν_1A_g)[a]	9.9(100)	7.2(100)	8.3(100)	8.2(100)	7.9(100)	7.9(100)
844(ν_3B_g)[a]	9.2(19)	6.2(38)	7.4(39)	7.3(26)	6.6(33)	7.3(31)
796(ν_3E_g)[a]	13.3(20)	8.2(35)	9.8(24)	9.1(30)	8.6(37)	8.9(36)
	FWHM of XRD diffraction peak 2θ (Intensity) (units: °(%))					
27.7(100)[b]	0.23(100)	0.22(100)	0.24(100)	0.26(100)	0.26(100)	0.24(100)
29.7(16)[b]	0.23(15)	0.21(15)	0.23(16)	0.25(15)	0.26(15)	0.25(14)
33.2(20)[b]	0.23(18)	0.23(18)	0.25(18)	0.26(19)	0.27(18)	0.26(19)

[a] [8].
[b] [19].

degree. This fact occurs because microwave heating in materials is closely related to their dielectric properties and defect structure diffusion behavior when it is under microwave environment [15]. The interaction between microwaves and matter takes place through the electric and magnetic fields vectors of the electromagnetic field in the microwave region, involving polarization and conduction processes. Absorption mechanisms have been identified in the interaction of microwaves with matter, e.g. dipole reorientation, and these interactions can provoke variations in order-disorder relation of material [25]. A model based on $[MoO_4]^{2-}$ tetrahedrons was proposed to explain these variations.

Initially, we assume that before the interaction of microwaves with matter, the $SrMoO_4$ had the ability to generate electron-hole pairs (e′–h˙) [26]. This phenomenon is caused by the existence of distorted $[MoO_4]_d/[SrO_8]_d$ clusters (intrinsic defects) by a Jahn-Teller instability into the scheelite-type tetragonal structure [27]. These defects are able to polarize the lattice and lead to the electronic transitions between $½MoO_{4d} = ½SrO_{8d}$ (disordered clusters) and $½MoO_{4o} = ½SrO_{8o}$ (ordered clusters). When the microwave is absorbed by the clusters, the following process can occur:

$$SrMoO_{4(defects)} \rightarrow [MoO_4]_d^x + [MoO_4]_o^y + [SrO_8]_d^x + [SrO_8]_o^y \quad (2)$$

consequently, microwave radiation can make order of clusters higher, as observed between SMO-1 and SMO-2 (Table 5). The microwave field can be concentrated at the neck region of two contacted particles [15]; the use of capping agent can be modified away from formation of the SMO crystalline centers, acting as a modifier of surface and defects, and, consequently as modifier of the disorder-order relation because it modifies the contact between particles (SMO-2 to SMO-6).

In the molecular orbitals of a tetrahedral MoO_4^{-2} cluster to scheelite materials, following the approach of Zhang et al. [27] and Thongtem et al. [1], the valence band VB (t_1 symmetry), the Highest Occupied Molecular Orbital HOMO, has been formed from the O $2p_\pi$ states, and, the conduction band CB (e^* symmetry), Lowest Unoccupied Molecular Orbital LUMO, has been formed from an antibonding combination of Mo $4d_{(e)}$ state with O $2p_\pi$ states.

The electronic band structure HOMO-LUMO of the SMO, before $\lambda\nu$ excitation and after excitation with recombination (e′–h˙) electron-hole pair are presented in Fig. 5. In the fundamental state system, in semiconductors materials, the electrons are present in VB and holes in CB (Fig. 5(a)). In excited state system (absorption of photon energy $\lambda\nu$), an electron-hole pair is created, called an "exciton", where some electrons are promoted from t_1 molecular orbital (t_1 MO - HOMO) (predominately O $2p_\pi$ states) to e^* molecular orbital (e^*MO - LUMO) (combination between Mo $4d_{(e)}$ with O $2p_\pi$ states) and will occupy the conduction band CB (Fig. 5(b)). To conclude, the electrons in CB are combined with holes in valence bands VB to produce photon energy ($\lambda\nu'$) emission (Fig. 5(c)) [1,28,29]. Defects can occur when a material is reduced crystalline size to reduce the surface energy [29]. It is

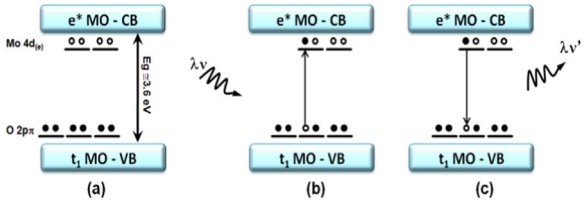

Fig. 5. The electronic band structure of the SMO: before $\lambda\nu$ excitation (a), and after excitation with recombination (e′–h˙) electron-hole pair and consequent photoluminescent emission (b, c). MO: molecular orbital; VB: valence band; CB: conduction band; •: electron;◯: hole.

expected that band gap and defects increase with a decrease in the size of the material [29]. This process can explain the optical properties of $SrMoO_4$ samples that will be presented below. Schematic representation in Fig. 5 shows clearly that SMO samples present optical properties, e.g. photoluminescence, if a photon energy $\lambda\nu$ surpass the energy barrier of the band gap (Eg).

Fig. 6 presents diffuse reflectance spectra of the SMO samples obtained between 200 and 800 nm. The SMO powders do not have transmittance properties, therefore 100% of excitation energy inserted in a sample, in optical reflectance measure, are the amount of reflectance and absorbance energies. All the SMO samples showed less reflectance, and consequently more absorbance, around of 270 nm (4.6 eV), and an additional shoulder around of 220 nm (5.6 eV). The band around 282 nm (4.4 eV) was attributed to electronic transitions within the MoO_4^{2-} complex, according to Spassky et al. [30] and other results of research already published by our group [11,21,31]. It can be seen that between 350 and 800 nm region the absorbance is poor and reflectance is high, but a less band of absorbance is observed around of 380 nm (3.3 eV), however, an association of these absorption is dubious. It probably happens due to the electronic transitions within MoO_4^{2-} complex without contribution from the Sr^{2+} [30]; however, in similar structure ($BaWO_4$), reflection peak was associated with the creation of the excitonic state in Ba^{2+} [32]. In this region of 350–800 nm (3.5–1.5 eV) approximately 80% of excitation energy inserted in a sample was emitted in the form of reflectance and 20% was absorbed. In SMO-1 bands around of 590–680 nm were observed, the presence of fringes in reflectance spectra (UV–vis region) is a characteristic feature of semiconductor materials and of order-disorder degree. The level of a disorder can promote a sprouting of sub-levels between a CB and VB, this promotion provokes the variation in energy amount to overcome band gap (characteristic of semiconductor materials). A small energy to overcome in band gap favors the excitation of electron and the absorption process in reflectance spectrum. However, the intensity of absorption in 590–680 nm is a smaller amount in comparison with the intensity of absorption in 270 nm, around of 20% and 88%, respectively, therefore, it is expected that the region in

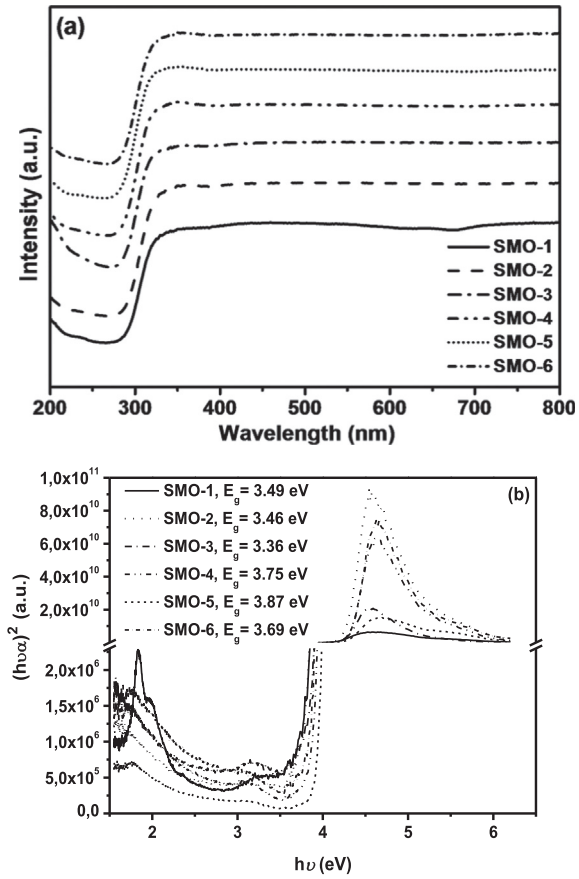

Fig. 6. (a) Reflectivity spectra recorded in the 200–800 nm (1.50–6.25 eV) range of SMO. (b) Tauc plots of SMO samples.

270 nm can be more efficient to excitation of material. And the fact is because band gap in $SrMoO_4$ is estimated near to 4.0 eV (310 nm) [14].

The diffuse reflectance spectra were translated into the absorption spectra by the Kubelka-Munk method. Kubelka-Munk's equation is described as follows: $\alpha = (1\text{-}R)^2/2R$, where α is the absorption coefficient and R the reflectivity. This conversion is available to estimate the band gap from powder diffuse reflection spectra [33–35]. The conversion of wavelength to energy scale for quantitative analysis was obtained by Jacobian Conversion, outlined by Mooney & Kambhampati [36].

The band gap energy can be determined using the Tauc relation: $\alpha \propto (h\nu - E_g)^n$, where E_g is the band gap energy, $h\nu$ is energy of photon and n is an index which assumes the values 1/2, 3/2, 2 and 3 depending on the nature of electronic transition responsible for the reflection [31,37]. The Tauc relation plot is plotted with $h\nu$ along the X-axis and $(h\nu\alpha)^2$ along the Y-axis; the direct band gap is found by extrapolating the X axis (where $n = 2$). The indirect band gap is found by Tauc relation plot, with $h\nu$ along the X-axis and $(\alpha)^{1/2}$ along the Y-axis; extrapolating the X axis (where $n = 1/2$). Direct and indirect band gap of all samples were calculated and obtained values are closed. However, in the theoretical study of Zhang et al. [27], the $CaMoO_4$ has the direct band gap, and this characteristic was assumed by $SrMoO_4$. The band gap energy values of SMO samples calculated using the Tauc relation are summarized in Table 3. More ordered structures are expected to have higher band gap energy than less ordered structures because defects promote intermediate stages between conduction and valence bands which decrease gap energy values [31]. The SMO samples, except SMO-1, were produced in same temperature, consequently, greater different in order-disorder was not expected, discussed previously by FWHM values from Bragg reflections and Raman bands (Table 5). However, with variation of capping agent, difference in morphology of particles surface was expected. When a material is truncated at the surface, the surface atoms have unsatisfied valences and, to reduce the surface energy, surface reconstructs occurs which leads to energy levels in the forbidden gap of the semiconductor, occurring the defects [29]. These defects can degrade the optical properties of the material.

It is expected that band gap and defects increase with a decrease in the size of the material, therefore the energetic gap necessary to occur recombination (e′–h˙) electron-hole pair can be variable, and, therefore, PL emission property can be altered (Fig. 5) [29]. In this work were observed these tendencies, according to this theory; SMO-5 have small crystallite size (31 nm), higher band gap calculated between SMO samples (3.87 eV) and probable more presence of defects damaging photoluminescence process. The opposite occur with SMO-1 and SMO-2, both present crystallite size around of 36 nm, band gap in 3.46 eV and probable less presence of defects, favoring the photoluminescence process. The scheelite material, as well as the molybdate group, possess intrinsic defects that can originate PL emission. The PL spectrum is another powerful tool to provide important information about the physical properties of materials at the molecular level, including shallow and deep level defects. A pure materials with higher-ordered (crystalline materials) or with higher defect density structures (amorphous materials) present unfavorable conditions for intense PL emission due to the superior energy necessary to surpass band gap [24].

Fig. 7 illustrates PL spectra (argon-ion laser with λ_{exc} 350.7 nm (3.53 eV)) obtained at room temperature for $SrMoO_4$ samples where a broadband, covering the visible electromagnetic region from 400 to 700 nm, is observed. This band type is characteristic of a multi-phonon and multi-level process; e.g., a system in which relaxation occurs by several paths involving the participation of numerous states within the material band gap. All SMO samples present PL emission (Fig. 7a), however, a broadband is variable, and, two main effects are proposed based on similar events. The first effect is a consequence of structural factors in the scheelite as the intrinsic distortion, asymmetric distortion $[MoO_4]$ tetrahedra and $[SrO_8]$ octahedra [24,37]. The asymmetric distortion allows the interaction between electrons and holes, favoring the luminescence phenomena. The second effect is a result of the surface defect (degree of aggregation and alignment between particles), generated by morphological control, which modifies PL emissions because of a formation of defects [29].

In relation to the profile of the curve, it is possible to observe that a delocalization of multi-level process density in a visible electromagnetic region is linked to the formation process of material obtained. PL curves of SMO-1, SMO-2, SMO-3, SMO-4, SMO-5 and SMO-6 have a maximum at 537 nm (2.31 eV), 470 nm (2.64 eV), 510 nm (2.43 eV), 448 nm (2.77 eV), 506 nm (2.45 eV) and 446 nm (2.78 eV), respectively. The sequence of delocalization in a visible electromagnetic region of red to blue in samples was: SMO-1; SMO-3∼SMO-5; SMO-2; SMO-4∼SMO-6. The sequence of relative intensity of higher to less was: SMO-1; SMO-2; SMO-3; SMO-4∼SMO-6; SMO-5 (near to null). The SMO-1 sample presented a broadband with a predominance of yellow PL emission (∼537 nm; 2.31 eV); and this emission was the higher intensity of all samples (Fig. 7a). SMO-4 and SMO-6 sample show a band maximum dislocated to the green-blue emission around of 447 nm (2.77 eV), which is the region of higher transition energy; with less intensity. SMO-2, SMO-3, and SMO-5 samples also present a broadband but with a band maximum dislocated to the green-yellow emission around of 499 nm (2.51 eV) and SMO-5 showed be near to null.

PL experimental curves were converted of wavelength to energy scale by Jacobian Conversion for quantitative analysis using the PeakFit deconvolution program [36,38]. The intention was to expand an understanding of PL properties and their dependence on the lattice structural order-disorder. Assuming PL emission peaks can be described with a Gaussian function; the PL emission can be fitted by multiple peaks and analyzed. This deconvolution and the areas under the curve of the respective transitions are illustrated in Fig. 7b.

$SrMoO_4$ PL curves for samples are composed of six PL components: blue, blue-green, green, yellow, orange and red, with maximum about

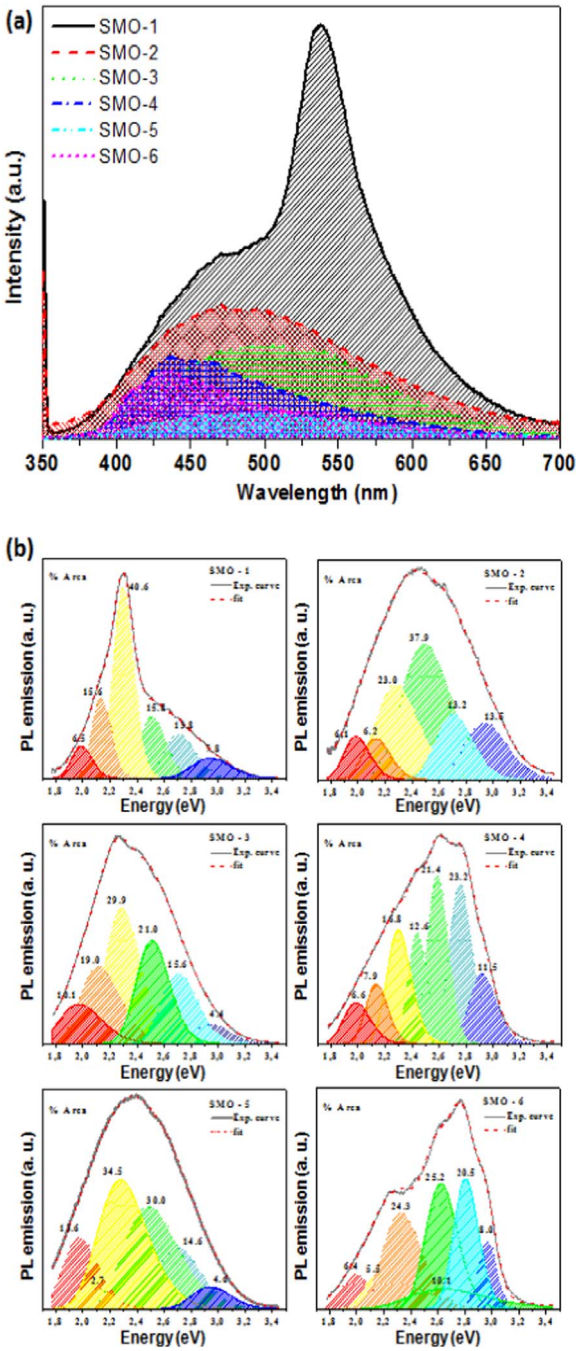

Fig. 7. (a) Room-temperature PL spectra of SMO powders. (b) Room-temperature PL spectra, deconvolution of PL curves fitted and area percentage of fitting parameters for SMO powders excited with the 350.7 nm wavelength of an argon-ion.

of 2.96 eV, 2.72 eV, 2.52 eV, 2.30 eV, 2.14 eV and 1.99 eV respectively. PL curves of SMO-4 and SMO-6 samples were better decompounded in seven PL components; in these PL curves, the green component (2.52 eV) was sliced in two green components, with maximum of about 2.59 eV and 2.44 eV.

A color is linked to a different type of electronic transition and represents a specific structural arrangement. A yellow-orange-red emission is linked to a disordered structure with deep defects, and a blue-green emission is linked to an ordered structure with shallow defects [39]. The decrease of areas designated as yellow, orange and red in PL spectra followed by an increase of the areas designated as green and blue are known as the representative of a supplementary ordered structure.

All samples present less contribution in extremes of electromagnetic spectra in the visible region (red and violet emission); the contribution in red, orange and blue region were around 9% each, however a contribution in green-blue, green and yellow were bigger, around of 17%, 29%, and 28%, respectively. The PL deconvolution results indicate that the sample which was produced without MAH treatment and without capping agent, SMO-1, presented a greater contribution in yellow region (40.5%). The crystallite size of the SMO-1 showed be a bigger of all samples, therefore are expected a less surface and depth defect, and lower band gap, favoring the PL properties in red region of electromagnetic spectra [29].

The PL deconvolution profile of samples SMO-4 and SMO-6 indicates a considerable increase in energy states related to low defects due to the high band intensity located between 2.82 and 2.64 eV (blue-green/green emission), corresponding to around 56.5% of all emission. The delocalization of emission to blue region of electromagnetic spectra is linked to the structural order increase and is associated with shallow defects and disorder which is linked to deep defects inserted in the band gap [24]. These deep defects suppresses the photoluminescent property, decreasing the intensity. These PL deconvolution results of SMO are in accordance with gap values obtained (Table 3).

To gain a better understanding of possible color emission and their dependence on the lattice structural order-disorder, PL curves were analyzed using the CIE (Commission Internationale de I'Eclairage 1931 chromaticity) coordinates positions (Fig. 8), which show the different emission colors for the as-synthesized SMO-1, SMO-2, SMO-3, SMO-4, SMO-5 and SMO-6, respectively.

It can be seen that all samples can emit bright yellow light, with fewer variations of coordinate positions. The SMO-1 sample can emit bright yellow-orange light and its chromaticity coordinates are x = 0.4184 and y = 0.4173. The SMO-2 sample can emit light yellow color, which chromaticity coordinates are x = 0.3920, and y = 0.4098. The SMO-3 and SMO-5 samples show the luminescence color similar to SMO-1; emission is bright yellow-orange; the chromaticity coordinates are x = 0.4512, and y = 0.4315 and x = 0.4270, and y = 0.4271, respectively. Chromaticity coordinates are x = 0.3967, and y = 0.4609 to SMO-4 sample, it can emit green-orange light. The SMO-6 sample can emit green color, which chromaticity coordinates are x = 0.3562, and y = 0.4481. The analysis of CIE coordinate positions data confirm the results of a band gap and optical properties. SMO-1 showed bigger crystallite size, less surface and depth defect and lower band gap, favoring PL curve delocalized in yellow region (maximum at 537 nm) and CIE coordinate located in red region that is a spectra region of less energy, while that SMO-6 possesses band gap of around 3.87 eV, PL curve dislocated to the green-blue region (maximum at 446 nm) and presented CIE coordinates in green region (higher energy).

From the combination of characterizations it was observed that microwave radiation favors an organization of material, but this organization can be changed after the use of capping agent that provokes

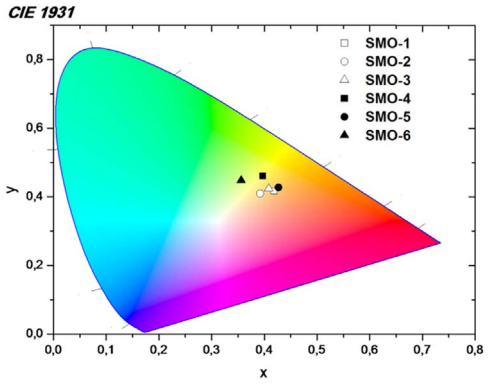

Fig. 8. CIE coordinates positions data for SMO micro-crystals.

alterations in morphology, in crystalline size and in disorder-order degree. These alterations provoke surface defect states that promote formation of defects and variations of the band gap of the material; it favors an alteration in PL emission. If the surface state is controlled, the particle size and morphology can be restricted deeply and shallow defects can be controlled and the properties of the PL can be modified according to what is desired.

4. Conclusions

In summary, strontium molybdate particles ($SrMoO_4$) were prepared by MAH method with variations in applied experimental parameters. Scheelite-type single crystalline structures of $SrMoO_4$ were identified by XRD, Raman, and FTIR. Formation crystals type coral sea were characterized by microscopy FE-SEM. The microwave radiation favors an organization of material, but this organization can be changed after the use of capping agent that provokes alterations in morphology, in crystalline size and in disorder-order degree. Values of band gap energy were between 3.36 eV and 3.87 eV, according to a disorder-order degree of a sample. This study indicates that surface defect states and variations of the band gap of the material favor an alteration in PL emission. If the surface state is controlled, the particle size and morphology can be restricted deeply and shallow defects can be controlled and the properties of the PL can be modified according to what is desired.

Acknowledgment

Grant #2013/07437-5, #2016/20568-5 São Paulo Research Foundation (FAPESP). The authors acknowledge the support of Brazilian agencies CNPq, FAPESP-CEPID, and CAPES. In memory of M. F. C. Abreu.

References

[1] T. Thongtem, A. Phuruangrat, S. Thongtem, Microwave-assisted synthesis and characterization of $SrMoO_4$ and $SrWO_4$ nanocrystals, J. Nanopart. Res. 12 (2010) 2287–2294.
[2] E. Ciftyürek, K. Sabolsky, E.M. Sabolsky, Molybdenum and tungsten oxide based gas sensors for high temperature detection of environmentally hazardous sulfur species, Sens. Actuators B 237 (2016) 262–274.
[3] J. Kubo, W. Ueda, Catalytic behavior of AMoO(x) (A = Ba, Sr) in oxidation of 2-propanol, Mater. Res. Bull. 44 (2009) 906–912.
[4] Y. Wang, S.L. Gai, C.X. Li, X. Zhang, N. Niu, F. He, M.L. Zhang, P.P. Yang, Controlled synthesis and luminescent properties of uniform $SrMoO_4$ hollow microstructures and application as drug carrier, RSC Adv. 3 (2013) 5945–5955.
[5] D. Li, Y. Wang, X. Zhang, G. Shi, G. Liu, Y. Song, White upconversion emission in $Yb^{3+}/Tm^{3+}/Ho^{3+}$ doped $SrMoO_4$ nanocrystals by high excited state energy transfer, J. Alloy. Compd. 550 (2013) 509–513.
[6] H. Yu, Z. Li, A.J. Lee, J. Li, H.J. Zhang, J.Y. Wang, H.M. Pask, J.A. Piper, M.H. Jiang, A continuous wave $SrMoO_4$ Raman laser, Opt. Lett. 36 (4) (2011) 579–581.
[7] C. Pupp, R. Yamdagni, R.F. Porter, Mass spectrometric study of the evaporation of $BaMoO_4$ and $BaWO_4$, J. Inorg. Nucl. Chem. 31 (7) (1969) 2021–2029.
[8] T.T. Basiev, A.A. Sobol, Y.K. Voronko, P.G. Zverev, Spontaneous Raman spectroscopy of tungstate and molybdate crystals for Raman lasers, Opt. Mater. 15 (3) (2000) 205–216.
[9] S.B. Mikhrin, A.N. Mishin, A.S. Potapov, P.A. Rodnyi, A.S. Voloshinovskii, X-ray excited luminescence of some molybdates, Nucl. Instrum. Methods Phys. Res. Sect. A 486 (1–2) (2002) 295–297.
[10] S.D. Ramarao, S.R. Kiran, V.R.K. Murthy, Structural, lattice vibrational, optical and microwave dielectric studies on $Ca_{1-x}Sr_xMoO_4$ ceramics with scheelite structure, Mater. Res. Bull. 56 (2014) 71–79.
[11] A.Pd.A. Marques, D.M.A. Melo, C.A. Paskocimas, P.S. Pizani, E.R. Leite, E. Longo, Study of the Photoluminescence $SrMoo_4$ Powders Synthesized by Complex Polymerization Method (CPM), in: A.M. Newman (Ed.), Focus on Solid State Chemistry, Nova Science Publishers, Inc, Hauppauge NY, 2006(117-13).
[12] Y. Zhang, F. Yang, J. Yang, Y. Tang, P. Yuan, Synthesis of crystalline $SrMoO_4$ nanowires from polyoxometalates, Solid State Commun. 133 (12) (2005) 759–763.
[13] N. Niu, P.A.P. Yang, W.X. Wang, F. He, S.L. Gai, D. Wang, J. Lin, Solvothermal synthesis of $SrMoO_4$:Ln (Ln = Eu^{3+}, Tb^{3+}, Dy^{3+}) nanoparticles and its photoluminescence properties at room temperature, Mater. Res. Bull. 46 (3) (2011) 333–339.
[14] J.C. Sczancoski, L.S. Cavalcante, M.R. Joya, J.A. Varela, P.S. Pizani, E. Longo, $SrMoO_4$ powders processed in microwave-hydrothermal: synthesis, characterization and optical properties, Chem. Eng. J. 140 (1–3) (2008) 632–637.
[15] M. Oghbaei, O. Mirzaee, Microwave versus conventional sintering: a review of fundamentals, advantages and applications, J. Alloy. Compd. 494 (1–2) (2010) 175–189.
[16] D.K. Agrawal, Microwave processing of ceramics, Curr. Opin. Solid State Mater. Sci. 3 (1998) 480–485.
[17] P. Yadoji, R. Peelamedu, D. Agrawal, R. Roy, Microwave sintering of Ni–Zn ferrites: comparison with conventional sintering, Mater. Sci. Eng., B98(3) 269–278.
[18] A.P.A. Marques, F.C. Picon, D.M.A. Melo, P.S. Pizani, E.R. Leite, J.A. Varela, E. Longo, Effect of the order and disorder of $BaMoO_4$ powders in photoluminescent properties, J. Fluoresc. 18 (1) (2008) 51–59.
[19] JCPDS No 08-0482.
[20] G. Hitoki, T. Takata, S. Ikeda, M. Hara, J.N. Kondo, M. Kakihana, K. Domen, Mechano-catalytic overall water splitting on some mixed oxides, Catal. Today 63 (2–4) (2000) 175–181.
[21] A.P.A. Marques, M.T.S. Tanaka, E. Longo, E.R. Leite, I.L.V. Rosa, The role of the Eu^{3+} concentration on the $SrMoO_4$: Eu phosphor properties: synthesis, characterization and photophysical studies, J. Fluoresc. 21 (3) (2011) 893–899.
[22] K. Nakamoto, Infrared and Raman Spectra of Inorganic and Coordination Compounds, Wiley, New York, 1986.
[23] M.R. Moura, A.P. Ayala, I. Guedes, M. Grimsditch, C.K. Loong, L.A. Boatner, Raman scattering study of $Tb(V_{1-x}P_x)O^{-4}$ single crystals, J. Appl. Phys. 95 (3) (2004) 1148–1151.
[24] M.F.C. Abreu, F.V. Motta, R.C. Lima, M.S. Li, E. Longo, A.Pd.A. Marques, Effect of process parameters on photophysical properties and barium molybdate phosphors characteristics, Ceram. Int. 40 (5) (2014) 6719–6729.
[25] D.K. Agrawal, Microwave processing of ceramics, Curr. Opin. Solid State Mater. Sci. 3 (1998) 480–485.
[26] L.S. Cavalcante, J.C. Sczancoski, N.C. Batista, E. Longo, J.A. Varela, M.O. Orlandi, Growth mechanism and photocatalytic properties of $SrWO_4$ microcrystals synthesized by injection of ions into a hot aqueous solution, Adv. Powder Technol. 24 (1) (2013) 344–353.
[27] Y. Zhang, N.A.W. Holzwarth, R.T. Williams, Electronic band structures of the scheelite materials $CaMoO_4$, $CaWO_4$, $PbMoO_4$, and $PbWO_4$, Phys. Rev. B: Condens. Matter 57 (20) (1998) 12738–12750.
[28] J.C. Sczancoski, L.S. Cavalcante, M.R. Joya, J.W.M. Espinosa, P.S. Pizani, J.A. Varela, E. Longo, Synthesis, growth process and photoluminescence properties of $SrWO_4$ powders, J. Colloid Interface Sci. 330 (1) (2009) 227–236.
[29] T. Pradeep, Nano: the Essentials, Understanding Nanoscience and Nanotechnology, McGraw-Hill, New York, 2007.
[30] D.A. Spassky, S.N. Ivanov, V.N. Kolobanov, V.V. Mikhailin, V.N. Zemskov, B.I. Zadneprovski, L.I. Potkin, Optical and luminescent properties of the lead and barium molybdates, Radiat. Meas. 38 (4–6) (2004) 607–610.
[31] A.P. de Azevedo Marques, E.R. Leite, J.A. Varela, E. Longo, Effect of variations in annealing temperature and metallic cations on nanostructured molybdate thin films, Nanoscale Res. Lett. 3 (4) (2008) 152–157.
[32] V.N. Kolobanov, I.A. Kamenskikh, V.V. Mikhailin, I.N. Shpinkov, D.A. Spassky, B.I. Zadneprovsky, L.I. Potkin, G. Zimmerer, Optical and luminescent properties of anisotropictungstate crystals, Nucl. Instrum. Methods A 486 (2002) 496–503.
[33] K. Suzuki, K. Kijima, Optical band gap of barium titanate nanoparticles prepared by RF-plasma chemical vapor deposition, Jpn. J. Appl. Phys. 44 (2005) 2081–2082.
[34] C.H. Park, D.A. Keszler, H. Yanagi, J. Tate, Gap modulation in $MCuQ_{1-x}Q'_xF$ (M = Ba, Sr; Q, Q′ = S, Se, Te) and related materials, Thin Solid Films 445 (2) (2003) 288–293.
[35] D.L. Wood, J. Tauc, Weak absorption tails in amorphous semiconductors, Phys. Rev. B: Condens. Matter 5 (8) (1972) 3144.
[36] J. Mooney, P. Kambhampati, Get the basics right: jacobian conversion of wavelength and energy scales for quantitative analysis of emission spectra, J. Phys. Chem. Lett. 4 (2013) 3316–3318.
[37] V.M. Longo, A.T. de Figueiredo, S. de Lázaro, M.F. Gurgel, M.G.S. Costa, C.O. Paiva-Santos, J.A. Varela, E. Longo, V.R. Mastelaro, F.S. de Vicente, A.C. Hernandes, R.W.A. Franco, Structural conditions that leads to photoluminescence emission in $SrTiO_3$: an experimental and theoretical approach, J. Appl. Phys. 104 (2) (2008) 023515.
[38] T. Ding, W.T. Zheng, H.W. Tian, J.F. Zang, Z.D. Zhao, S.S. Yu, X.T. Li, F.L. Meng, Y.M. Wang, X.G. Kong, Temperature-dependent photoluminescence in $La_{2/3}Ca_{1/3}MnO_3$, Solid State Commun. 132 (12) (2004) 815–819.
[39] V.M. Longo, E. Orhan, L.S. Cavalcante, S.L. Porto, J.W.M. Espinosa, J.A. Varela, E. Longo, Understanding the origin of photoluminescence in disordered $Ca_{0.60}Sr_{0.40}WO_4$: an experimental and first-principles study, Chem. Phys. 334 (1–3) (2007) 180–188.